Domain Decomposition Methods in Electrothermomechanical Coupling Problems

Ronald H.W. Hoppe[1,2], Yuri Iliash[2], Siegfried Ramminger[3], and Gerhard Wachutka[4]

[1] University of Houston, Department of Mathematics (http://www.math.uh.edu/~rohop/)
[2] University of Augsburg, Institute for Mathematics (http://wwwhoppe.math.uni-augsburg.de)
[3] Siemens AG, Corporate Technology (http://www.mchp.siemens.de)
[4] Munich University of Technology, Physics of Electrotechnology (http://www.tep.e-technik.tu-muenchen.de)

Summary. In this contribution, we are concerned with electrothermomechanical coupling problems as they arise in the modeling and simulation of high power electronic devices. In particular, we are faced with a hierarchy of coupled physical effects in so far as electrical energy is converted to Joule heat causing heat stresses that have an impact on the mechanical behavior of the devices and may lead to mechanical damage. Moreover, there are structural coupling effects due to the sandwich-like construction of the devices featuring multiple layers of specific materials with different thermal and mechanical properties. The latter motivates the application of domain decomposition techniques on nonmatching grids based on individual finite element discretizations of the substructures. We will address in detail the modeling aspects of the hierarchy of coupling phenomena as well as the discretization-related couplings in the numerical simulation of the operating behavior of the devices.

1 Introduction

We consider the application of heterogeneous domain decomposition methodologies in the simulation of electrothermomechanical coupling problems. Such multiphysics coupling problems occur in many applications such as Micro-Electro-Mechanical-Systems (MEMS) and in high power electronics. In the latter case, a characteristic feature of the operational behavior of the devices and systems is that electric energy is converted to Joule heat causing heat stresses which in turn lead to deformations of the underlying mechanical structure and even to damage, if no appropriate cooling is provided.
Basically, the modeling is done in the macroscopic regime by using a continuum mechanical approach. On the other hand, failure mechanisms such as crack initiation and propagation strongly depend on microstructural details

which additionally are taken into account by means of an empirical crack model.
As algorithmic tools in the numerical simulation of the appropriately discretized coupled system of PDEs, we use adaptive multilevel methods and domain decompositions on nonmatching grids. As we shall see, the decomposition of the computational domain is in a natural way given by the geometrical structure of the devices featuring subdomains of strongly different aspect ratios and consisting of materials with largely different thermomechanical properties.
The paper is organized as follows: In Section 2, as an example for a device whose operational behavior is based on electrothermomechanical coupling, we consider an Integrated High Voltage Module. Section 3 provides the mathematical modeling of the coupling problem, whereas Section 4 addresses the algorithmic tools used in the numerical simulation. Finally, in Section 5 we present simulation results illustrating the distribution of the temperature and equivalence stresses as well as the initiation of cracks in critical parts of the module.

2 Integrated High Voltage Modules

In high power electronics, Integrated High Voltage (IHV) Modules are used as converters for high power electromotors. They consist of specific semiconductor devices, as for instance, Insulated Gate Bipolar Transistors (IGBTs) and power diodes serving as switches for the electric currents (see the topmost blocks in Figure 1 referred to as Ω_1 in the sequel).

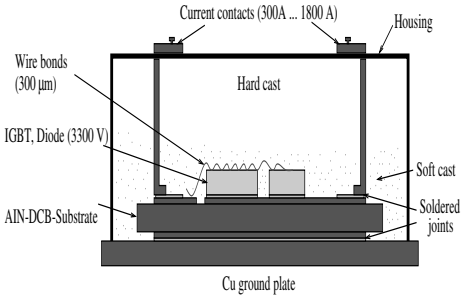

Fig. 1. Schematic representation of an Integrated-High-Voltage Module

Due to high currents up to several kiloamperes, electric energy is converted to Joule heat which leads to a considerable self-heating of the device. In order to facilitate an appropriate distribution of the heat, these blocks are fixed on several layers of different materials (copper and aluminum-nitride) attached to each other by thin soldered joints. The union of these blocks will be denoted

by Ω_2. Finally, the copper ground plate is mounted on a cooling device. With regard to failure, the critical parts of the device are the wire bonds connecting the current contacts with the semiconductor devices and the soldered joints.

3 The mathematical model

The operational behavior of the IHV Module involves processes on two different time scales: There is a fast time scale which is the operation of the semiconductor devices having switching times of less than 100 nanoseconds, and there is a slow time scale with regard to the temporal evolution of the temperature in the module which occurs in the range of minutes.
As a model simplification, these two processes are decoupled in the sense that the semiconductor device equations, considered in Ω_1, are treated first to compute the generated Joule heat as an input for the heat equation considered in Ω_2.
We use the classical drift-diffusion model consisting of a potential equation for the electric potential ψ that is coupled with the continuity equations for the carrier concentrations n and p where $\mathbf{J}_n$ and $\mathbf{J}_p$ denote the densities of the electrons and holes, respectively.

$$-\nabla \cdot \varepsilon \nabla \psi \; + \; N_{dop}(n,p) \; + \; q(n-p) \; = \; 0 \; , \tag{1}$$

$$\frac{\partial n}{\partial t} \; = \; + \, q^{-1} \nabla \mathbf{J}_n \; + \; G(\mathbf{J}_n, \mathbf{J}_p, \mathbf{E}) \; - \; R(n,p) \; , \tag{2}$$

$$\frac{\partial p}{\partial t} \; = \; - \, q^{-1} \nabla \mathbf{J}_p \; + \; G(\mathbf{J}_n, \mathbf{J}_p, \mathbf{E}) \; - \; R(n,p) \; , \tag{3}$$

$$\mathbf{J}_n \; = \; - \, q \; \mu_n \; n \; \nabla \psi \quad , \quad \mathbf{J}_p \; = \; - \, q \; \mu_p \; p \; \nabla \psi \; . \tag{4}$$

Here, q stands for the elementary charge, whereas μ_n and μ_p refer to the mobilities of the electrons and holes. Moreover, $\mathbf{E} = -\nabla\psi$ is the electric field whereas N_{dop} , G and R refer to the doping profile, the generation and the recombination. The dominant heat source is Joule heat $H_J = |\mathbf{J}_n|^2/(q\mu_n n) + |\mathbf{J}_p|^2/(q\mu_p p)$, while other sources based on the Seebeck and Nernst effect can be neglected.
The temporal and spatial distribution of the temperature T is described by the heat equation considered in the domain Ω_2 occupied by the aluminum-nitride and copper blocks as well as the joints.

$$\rho \; c \; \frac{\partial T}{\partial t} = \nabla \cdot (\kappa \; \nabla T) \quad \text{in } Q_2 := \Omega_2 \times (t_0, t_1) \quad , \tag{5}$$

$$\mathbf{n} \cdot \kappa \; \nabla T = H_J(t) \quad \text{on } \Gamma_0 \times (t_0, t_1) \quad , \tag{6}$$

$$\mathbf{n} \cdot \kappa \; \nabla T = h \; (T^* - T) \quad \text{on } \Gamma_1 \times (t_0, t_1) \quad , \tag{7}$$

$$\mathbf{n} \cdot \kappa \; \nabla T = 0 \quad \text{on } \Gamma_2 \times (t_0, t_1) \quad , \tag{8}$$

$$T(\cdot, t_0) = T_0(\cdot) \quad \text{in } \Omega_2 \quad . \tag{9}$$

Here, ρ , c, and κ stand for the density, heat capacity, and heat conductivity, respectively. The Joule heat through the part Γ_0 of the upper boundary of the computational domain Ω_2 attached to the semiconductor devices serves as the source term. We further assume a heat exchange at the lower boundary Γ_1 between the copper ground plate and the cooling device where h stands for the heat transition coefficient and T^* denotes the ambient temperature. On the other boundaries of Ω_2 we assume perfect insulation. We note that the thermal properties of the materials such as the heat capacity and the heat conductivity are quite different which means that we experience jumping coefficients across subdomain boundaries. As mentioned before, the self-heating of the devices leads to heat stresses causing mechanical deformations. For all parts of the module except the wire bonds and the joints, we assume the equations of linear elasticity:

$$\text{div}\ \boldsymbol{\sigma}(\mathbf{u}) \ = \ \frac{\alpha\ (1-\nu)\ E}{(1+\nu)\ (1-2\nu)}\ \nabla(T-T_0) \quad \text{in}\ \Omega_2 \quad , \tag{10}$$

$$\mathbf{u} \ = \ 0 \quad \text{on}\ \Gamma_1 \quad , \quad \mathbf{n}\cdot\boldsymbol{\sigma}(\mathbf{u}) \ = \ 0 \quad \text{on}\ \Gamma_0 \cup \Gamma_2 \quad . \tag{11}$$

Here, $\mathbf{u}$ and $\boldsymbol{\sigma}(\mathbf{u})$ stand for the displacement vector and the stress tensor. Moreover, α denotes the thermal expansion coefficient, and E and ν refer to Young's modulus and Poisson's ratio which are also strongly different for the various materials. The wire bonds and the solders are possibly subject to plastic deformation. Here, we assume stationary plasticity with the von Mises yield criterion where the set K of admissible stresses is given in terms of the Frobenius norm $\|\cdot\|_F$ of the deviatoric stress tensor and the von Mises yield stress σ_Y by $K := \{\sigma \mid \|\text{dev}(\sigma)\|_F \leq \sqrt{2/3}\ \sigma_Y\}$. The computational domains are those occupied by the wires and the joints, respectively.
Cracks typically occur in the bonding zone where the wires are attached to the chips and in the soldered joints ([Ramminger, Seliger, and Wachutka, 2000]). There exist empirical crack models that are based on macroscopic data combined with microstructural data due to the nucleation and growth of pores. For instance, the modified Gurson-Model ([Tvergaard, 1989]) consists of a flow rule that reduces to the von Mises yield rule in case of vanishing voids in the microstructure of the material:

$$\frac{\sigma_E^2}{\sigma_Y^2} \ - \ 1 \ + \ 2\ q\ f\ \cosh((2\sigma_Y)^{-1}\sigma_{ii}) \ - \ (q\ f)^2 \ = \ 0 \quad . \tag{12}$$

Here, σ_E refers to the von Mises equivalence stress and σ_Y stands for the yield stress whereas σ_{ii} is the trace of the Cauchy stress tensor. Moreover, f denotes the pore volume fraction and q is a material parameter.

In case of plastic deformation, micropores nucleate and grow at places of defects in the crystallographic structure. The pore evolution consists of two parts, namely the nucleation of pores and the growth of already existing

pores. For the latter, the growth rate is assumed to be proportional to the hydrostatic part of the stress tensor whereas the nucleation part is controlled by the plastic deformation. Altogether, this leads to an evolution equation for the pore volume fraction f:

$$\frac{\partial f}{\partial t} = (1-f)\ \frac{\partial \boldsymbol{\varepsilon}^p_{ii}}{\partial t} + d_N\ \exp(-\frac{1}{2}\ \frac{(\varepsilon^p_M - \varepsilon_N)^2}{s_N})\ \frac{\partial \varepsilon_N}{\partial t}\ ,\ f(t_0)\ =\ f_0\ . \quad (13)$$

Here, $\frac{\partial \boldsymbol{\varepsilon}^p_{ii}}{\partial t}$ is the trace of the plastic equivalent rate tensor, ε_N stands for the mean nucleation equivalent plastic strain and ε^p_M denotes the equivalent plastic strain of the matrix material. Moreover, s_N refers to the standard deviation and d_N is a material parameter depending on the volume fraction of void nucleating particles.

4 Algorithmic tools for numerical simulation

The discretization of the drift diffusion model (1)-(4) is done by conforming P1 elements for the potential equation and mixed hybrid finite elements involving the lowest order Raviart-Thomas elements $RT_0(K), K \in \mathcal{T}_h$, for the continuity equations with respect to an adaptively generated hierarchy of triangulations $\mathcal{T}_h$ of Ω_1. Denoting by $P_k(D), k \in \mathbb{N}_0$, the set of polynomials of degree k on D and by $\mathcal{F}_h^{int}$ the set of interior faces of $\mathcal{T}_h$, we set

$$\begin{aligned}
RT_0^{-1}(\Omega_1;\mathcal{T}_h)\ &:=\ \prod_{K\in\mathcal{T}_h} RT_0(K)\quad ,\\
W_0(\Omega_1;\mathcal{T}_h)\ &:=\ \{v_h : \Omega_1 \to \mathbb{R}\mid v_h|_K \in P_0(K)\ ,\ K\in\mathcal{T}_h\}\quad ,\\
M_0(\Omega_1;\mathcal{F}_h^{int})\ &:=\ \{\mu_h : \cup_{F\in\mathcal{F}_h^{int}} F \to \mathbb{R}\mid \mu_h|_F \in P_0(F)\ ,\ F\in\mathcal{F}_h^{int}\}\ .
\end{aligned}$$

The discretized continuity equations are solved by a Gummel type iteration where each iteration step requires the solution of the following problem (cf., e.g., [Brezzi, Marini, and Pietra, 1989]):
Find $(\mathbf{j}_h, u_h, \lambda_h) \in RT_0^{-1}(\Omega_1;\mathcal{T}_h)\times W_0(\Omega_1;\mathcal{T}_h)\times M_0(\Omega_1;\mathcal{F}_h^{int})$ such that for all $\mathbf{q}_h \in RT_0^{-1}(\Omega_1;\mathcal{T}_h)$, $v_h \in W_0(\Omega_1;\mathcal{T}_h)$, and $\mu_h \in M_0(\Omega_1;\mathcal{F}_h^{int})$ there holds

$$\begin{aligned}
&\sum_{K\in\mathcal{T}_h}\Big(\int_K a^{-1}\mathbf{j}_h\cdot\mathbf{q}_h dx + \int_K u_h\ \mathrm{div}\mathbf{q}_h dx - \sum_{F\in\mathcal{F}_h(K)}\int_F \lambda_h[\mathbf{n}_F\cdot\mathbf{q}_h]_J d\sigma\Big) = 0,\\
&\sum_{K\in\mathcal{T}_h}\Big(\int_K \mathrm{div}\mathbf{j}_h\ v_h dx - \int_K b u_h v_h\ dx\Big)\ =\ -\int_\Omega f v_h\ dx,\\
&\sum_{K\in\mathcal{T}_h}\sum_{F\in\mathcal{F}_h(K)}\int_F \mu_h\ [\mathbf{n}_F\cdot\mathbf{j}_h]_J d\sigma\ =\ 0\ .
\end{aligned}$$

Here, $[\mathbf{n}_F \cdot \mathbf{j}_h]_J$ denotes the jump of the normal component of $\mathbf{j}_h$ across innerelement faces $F \in \mathcal{F}_h(K)$. Static condensation of $\mathbf{j}_h$ and u_h in the resulting algebraic saddle point problem leads to a Schur complement system which can be shown to be equivalent to a nonconforming Petrov-Galerkin approach ([Brezzi, Marini, and Pietra, 1989]). Denoting by $CR_1(\Omega_1;\mathcal{T}_h)$ the lowest order nonconforming Crouzeix-Raviart space and by $B(\Omega_1;\mathcal{T}_h)$ the space of quartic bubble functions associated with each $K \in \mathcal{T}_h$, the problem is to find $u_{NC} \in CR_1(\Omega_1;\mathcal{T}_h) \oplus B(\Omega_1;\mathcal{T}_h)$ such that for all $v_h \in CR_1(\Omega_1;\mathcal{T}_h)$

$$\sum_{K\in\mathcal{T}_h} \int_K \Big[P_{a^{-1}}(a\ \nabla u_{NC}) \cdot \nabla v_h \ + \ b\ Pu_{NC}\ Pv_h \Big]\ dx \ = \ (Pf, v_h)_{0;\Omega_1}\ .$$

where $P : L^2(\Omega_1) \to W_0(\Omega_1;\mathcal{T}_h)$ and $P_{a^{-1}} : L^2(\Omega_1)^2 \to RT_0^{-1}(\Omega_1;\mathcal{T}_h)$ are the orthogonal L^2- resp. weighted L^2-projection. Taking advantage of this equivalence, a multilevel preconditioned iterative solver can be used, where the multilevel preconditioner is the associated conforming one, put into effect by transforming the nonconforming Crouzeix-Raviart space onto its conforming counterpart (for details as well as for the realized adaptive grid refinement based on a residual-type a posteriori error estimator we refer to [Hoppe and Wohlmuth, 1997]).

As far as the discretization of the thermomechanical coupling problem is concerned, we discretize in time by embedded Singly Diagonally Implicit Runge Kutta (SDIRK) methods. For discretization in space, we use domain decomposition methods on nonmatching grids. We consider a nonoverlapping, geometrically conforming decomposition $\Omega_2 = \cup_{i=1}^n \Omega_{2,i}\ ,\ \Omega_{2,i} \cap \Omega_{2,j} = \emptyset, 1 \le i \ne j \le n$, of the computational domain given by the sandwich like structure of the module (cf. Figure 1) and refer to $S = \cup_{i=1}^n (\partial\Omega_{2,i} \setminus \partial\Omega_2)$ as the skeleton of the decomposition. As we can see from the schematic representation of the IHV Module, we are faced with subdomains of different aspect ratios. Moreover, we know that the thermal and mechanical properties of the materials in the individual subdomains are quite different resulting in strongly discontinuous coefficient of the heat and mechanical equations across subdomain boundaries. Therefore, we use individual triangulations $\mathcal{T}_i$ of the subdomains $\Omega_{2,i}$ that do not necessarily match on the interfaces between adjacent subdomains and take care of the resulting nonconformity by mortar element methods based on discretizations of the subdomain problems by continuous, piecewise linear finite elements denoting by $S_{1,\Gamma_D}(\Omega_{2,i};\mathcal{T}_i)$ the associated finite element spaces. For $\Gamma_{ij} \subset S$, we refer to γ_{ij}^m and γ_{ij}^{nm} as the mortar and nonmortar inheriting its triangulations from $\mathcal{T}_i$ and $\mathcal{T}_j$, respectively. We construct the multiplier space $M_h(\gamma_{ij}^{nm})$ in the meanwhile standard way under special consideration of cross points. Setting $V_h = \prod_{i=1}^n S_{1,\Gamma_D}(\Omega_{2,i};\mathcal{T}_i)$ and $M_h = \prod_{\Gamma_{ij}\subset S} M_h(\gamma_{ij}^{nm})$, the mortar finite element approach reads as follows: Find $(u_h, \lambda_h) \in V_h \times M_h$ such that

$$a_h(u_h, v_h) \; + \; b_h(v_h, \lambda_h) = \ell(v_h) \; , \; v_h \in V_h \quad , \tag{14}$$

$$b_h(u_h, \mu_h) \qquad\qquad = \; 0 \; , \; \mu_h \in M_h \; , \tag{15}$$

where $a(\cdot,\cdot) : V_h \times V_h \rightarrow R$ is the bilinear form associated with the FE discretized subdomain problems and

$$b_h(v_h, \mu_h) \; = \; - \sum_{\Gamma_{ij} \subset S} \int_{\Gamma_{ij}} \mu_h \; [v_h]_J \; d\sigma$$

is the bilinear form that realizes the weak continuity constraints across the interfaces. The resulting algebraic saddle point problem is solved by multilevel preconditioned Lanczos iterations with a block diagonal preconditioner, where the first diagonal block consists of subdomain preconditioners, that can be chosen as, for instance, BPX-preconditioners for the discretized subdomain problems, and the second diagonal block is an interface preconditioner being spectrally equivalent to the Schur complement resulting from static condensation (for details we refer to [Hoppe, Iliash, Kuznetsov, Vassilevski, and Wohlmuth, 1998]).
The stationary plasticity problems for the joints and the wire bonds have been solved by the standard return-mapping algorithm.

5 Simulation results

Based on the mathematical models and the numerical methods described in the previous sections, we have performed simulations of the operational behavior of the IHV Module. Figure 2 displays the distribution of the temperature and the von Mises equivalence stresses in a cross section of the upper soldered joints. Temperature peaks of more than $100^0 C$ and the largest equivalence stresses occur in the center of the joints located below the IGBTs and power diodes. The simulation results are in good agreement with experimentally observed data.

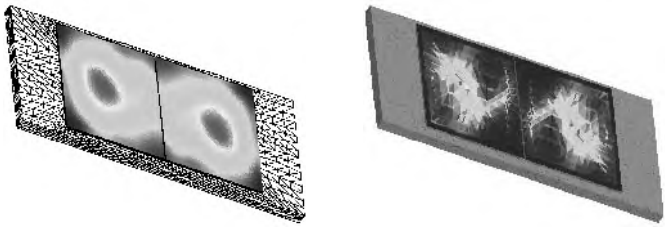

Fig. 2. Temperature distribution (left) and distribution of the equivalence stresses (right) in the upper soldered joint

We further consider the initiation and propagation of cracks in the wire bonding zone. Figure 3 shows a light microscopy of a crack opening in the wire bonding zone (left) as well as the plastic strain behavior at the beginning of the bonding zone (right) along the interface direction (solid lines) and perpendicular to it (dotted lines). Close to the crack tip, the wire is under tension in x-direction (upper curves) and under compression in y-direction (lower curves).

Acknowledgement. The work of the authors has been supported by the Federal Ministry for Education and Research (BMBF) under Grant No. 03HOM3A1.

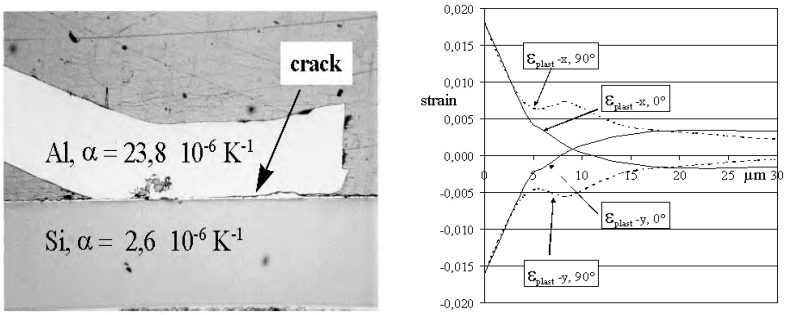

Fig. 3. Light microscopy of a crack (left) and the computed plastic strain at the beginning of the bonding zone (right)

References

F. Brezzi, D. Marini, and P. Pietra. Numerical simulation of semiconductor devices. *Comp. Math. Appl. Mech. Engrg.*, 75:493–514, 1989.

R. Hoppe, Y. Iliash, Y. Kuznetsov, Y. Vassilevski, and B. Wohlmuth. Analysis and parallel implementation of adaptive mortar element methods. *East-West J. Numer. Math.*, 6:223–248, 1998.

R. Hoppe and B. Wohlmuth. Adaptive multilevel techniques for mixed finite element discretizations of elliptic boundary value problems. *SIAM J. Numer. Anal.*, 34:1658–1681, 1997.

S. Ramminger, N. Seliger, and G. Wachutka. Reliability model for al wire bonds subjected to heel crack failures. *Microelectronics Reliability*, 40:1521–1525, 2000.

V. Tvergaard. Material failure by void growth to coalescence. *Advances in Applied Mechanics*, 27:83–151, 1989.